Nanotechnology and Nano-Interface Controlled Electronic Devices
Editors: M. Iwamoto, K. Kaneto and S. Mashiko

CHAPTER 7

Control of charge transfer and interface structures in nano-structured dye-sensitized solar cells

Shozo Yanagida, Takayuki Kitamura, and Yuji Wada

Department of Material and Life Science, Graduate School of Engineering, Osaka University, Yamada-oka 2-1, Suita, Osaka 565-0871, Japan

1. Introduction

Almost 10 years have passed since dye-sensitized solar cells (DSCs) were innovated by Grätzel's group [1–3]. DSCs can be constructed by Ruthenium complex [for example, N3 = *cis*-Ru^{II} $(dcbpy)_2(SCN^-)_2$ (dcbpy = 2,2′-bipyridine-4,4′-dicarboxylic acid); Scheme 1] dye-anchored nano-structured TiO_2 films and redox electrolyte made from iodine and iodide salts, and is currently under large, intense investigation, because

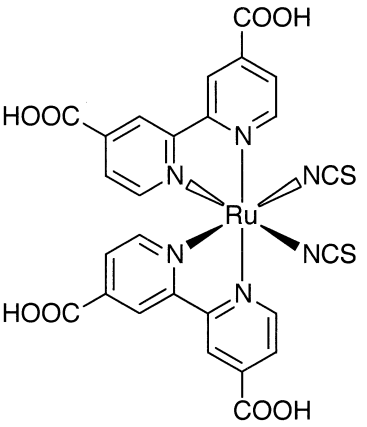

Scheme 1.

a DSC is noted to have the following advantages over silicon solar cells; respectable photo-conversion efficiency with high fill factor, low cost and earth-friendly materials (low material cost), economical production facilities like screen printing and ink jet printing (low labor cost), high open-circuit photovoltage at low light intensity that is favorable for indoor use, and less sensitiveness to angle of incidence of solar radiation which leads to an increase of total conversion of solar light per day. It is further interesting to note that a DSC permits the construction of transparent solar cell modules, so can be used in window and roof lighting.

The photoconversion efficiency can be obtained by measuring short circuit photocurrent density (J_{sc}), open-circuit photovoltage (V_{oc}) and fill factor (*ff*) under one sun irradiation (I_s) conditions (Eq. 1).

$$\eta = (J_{sc} \times V_{oc} \times ff)/I_s \tag{1}$$

The respectable photo-conversion efficiency can be explained by efficiency of light harvesting (η_{lh}) of the sensitizing Ru dye and efficiencies of transport of photo-formed electrons and holes in a DSC, i.e., η_e and η_h, as expressed by Eq. 2.

$$\eta = \eta_e \times \eta_{lh} \times \eta_h \tag{2}$$

The efficiency of transport of the photo-formed electrons can be subdivided in three factors, i.e., efficiency of electron injection from the excited dye molecule, η_{ei}, efficiency of electron transport in nano-structured TiO_2 phase, η_{et}, and efficiency of electron collection at the transparent electrode, η_{ec}, as expressed by Eq. 3.

$$\eta_e = \eta_{ec} \times \eta_{et} \times \eta_{ei} \tag{3}$$

The efficiency of transport of the photo-formed holes can be shown as a product of the efficiency of hole injection into the electrolyte as a hole-transport phase, η_{hi}, efficiency of charge (hole) transport in the electrolyte phase, η_{ht}, and efficiency of hole collection at the counter electrode, η_{hc} (Eq. 4).

$$\eta_h = \eta_{hi} \times \eta_{ht} \times \eta_{hc} \tag{4}$$

In a DSC, the seven factors must be well balanced to achieve the high efficiency. With regard to η_{lh} of the N3 dye, incident photon to current efficiency (IPCE) is almost 100% in the wide absorption band, which is comparable to amorphous silicon solar cells. This is due to the high absorption coefficient of N3 dye molecules and large ratio (>1000) of the nano-structured TiO_2 surface (mesoporous surface) area to the projected one defined as roughness factor.

Current research topics to improve DSCs are electron transfer dynamics that determine η_{ei} and η_{hi}, charge transport mechanism in mesoporous nano-crystalline TiO_2 phase referring to η_{et}, and mastering the interfaces that control η_{ec} and η_{hc}.

In this article, we will report how to improve the DSC efficiency in view of the above-mentioned factors. The charge transport efficiencies of both nano-structured TiO_2 and electrolyte solution, and electron transport at interfaces of window electrode and counter electrode will be discussed. On the basis of mechanistic points of view, we will propose some concepts for solidification of hole transporting phases.

2. Light harvesting efficiency based on dynamics of dye-sensitization

The dynamics of the interfacial electron-transfer from excited state of dye, N3, to TiO_2 was examined precisely by laser-induced ultra-fast transient spectroscopy as summarized in Fig. 1 [4–9]. These kinetics are largely affected by the composition of the electrolyte. For example, since decrease of surface pH makes the flat band potential positive, the presence of Li^+, which acts like H^+, leads it to the positive side, while the

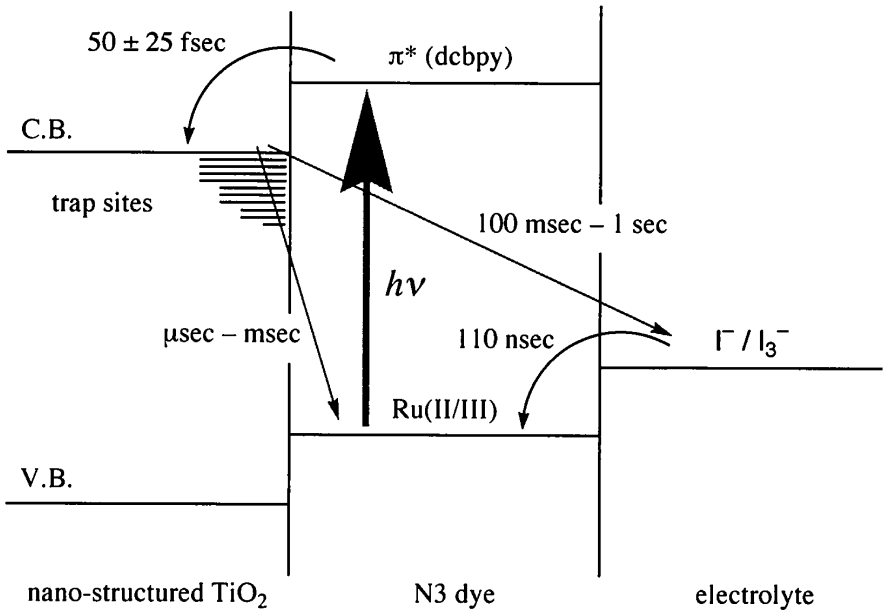

Fig. 1: Electron transfer dynamics at the interfaces of nano-structured TiO_2/N3 and N3/iodide electrolyte.

presence of basic pyridine derivatives shifts it to the negative side [10]. Concentrations of I^- and I_3^- formed by equilibrium of $I^- + I_2 \leftrightarrow I_3^-$ is also noted to affect charge transfer kinetics. At the efficient DSC conditions, however, the two forward electron-transfer steps are much faster than the corresponding reverse electron-transfer steps (charge recombination), by a factor of 10^6 to 10^9. The high conversion efficiency well explains effective and vectorial electron transfer in a DSC with N3, suggesting high values of η_{ei} and η_{hi}.

3. Electron transport in nano-structured TiO_2 electrodes

3.1. Ambipolar electron diffusion mechanism

The porous TiO_2 films of 10 μm-thickness formed by sintering av. 20 nm-sized TiO_2 particles have more than 500 boundaries across the film. The resulting nano-structured TiO_2 films have a large volume of pores inside with a porosity of 45 to 60%, giving a large surface area for dye-adsorption. Accordingly, the high efficiency of the DSC suggests that the nano-structured dye-coated TiO_2 films should exhibit high η_{et}, i.e., anomalous electron transport properties. Interestingly, such electron transporting properties of the nano-structured TiO_2 films should appear only when the films are filled with highly ionic electrolyte.

Electron transport in nano-structured TiO_2 films in a liquid electrolyte has been described in terms of carrier diffusion due to a lack of large electric field gradient in the film [11–26]. The diffusion coefficients of the dye-coated TiO_2 and the plain TiO_2 electrodes were reported to depend on light intensities, ranging from 10^{-8} to 10^{-4} $cm^2\,s^{-1}$. A trapping model [13,21,24–26] can well explain such slow diffusion of electrons, where electrons spend a large fraction of transient time in traps, as shown in Fig. 2.

According to the model, the number of traps, their energy distribution, and the steady state population of the trapped electrons affect the diffusion coefficients. For the nano-structured electrodes, the effect of traps is significant since the number of traps is extremely large due to the high surface area and boundaries where traps likely exist. It is interesting to note that other factors, which affect measured diffusion coefficients, are the concentration and diffusion coefficient of ions in an electrolyte. The effects of electrolyte ion concentrations on measured diffusion coefficient were reported by Solbrand et al. [19]. The diffusion coefficient and total amount of charges decreased as the electrolyte concentration decreased. Kopidakis et al. proposed an ambipolar diffusion mechanism to interpret the effect of electrolyte on the electron transport in a mesoporous TiO_2–electrolyte system [23]. Photoinjected electrons in TiO_2 were surrounded by an electrolyte consisting of various kinds of ionic species. The ambipolar diffusion coefficient is expressed by

$$D_{amb} = \frac{(n+p)}{(n/D_p)+(p/D_n)} \tag{5}$$

where n and p are the density of electrons and cations, and D_n and D_p are the diffusion coefficients of electrons and cations, respectively. The diffusion coefficient of

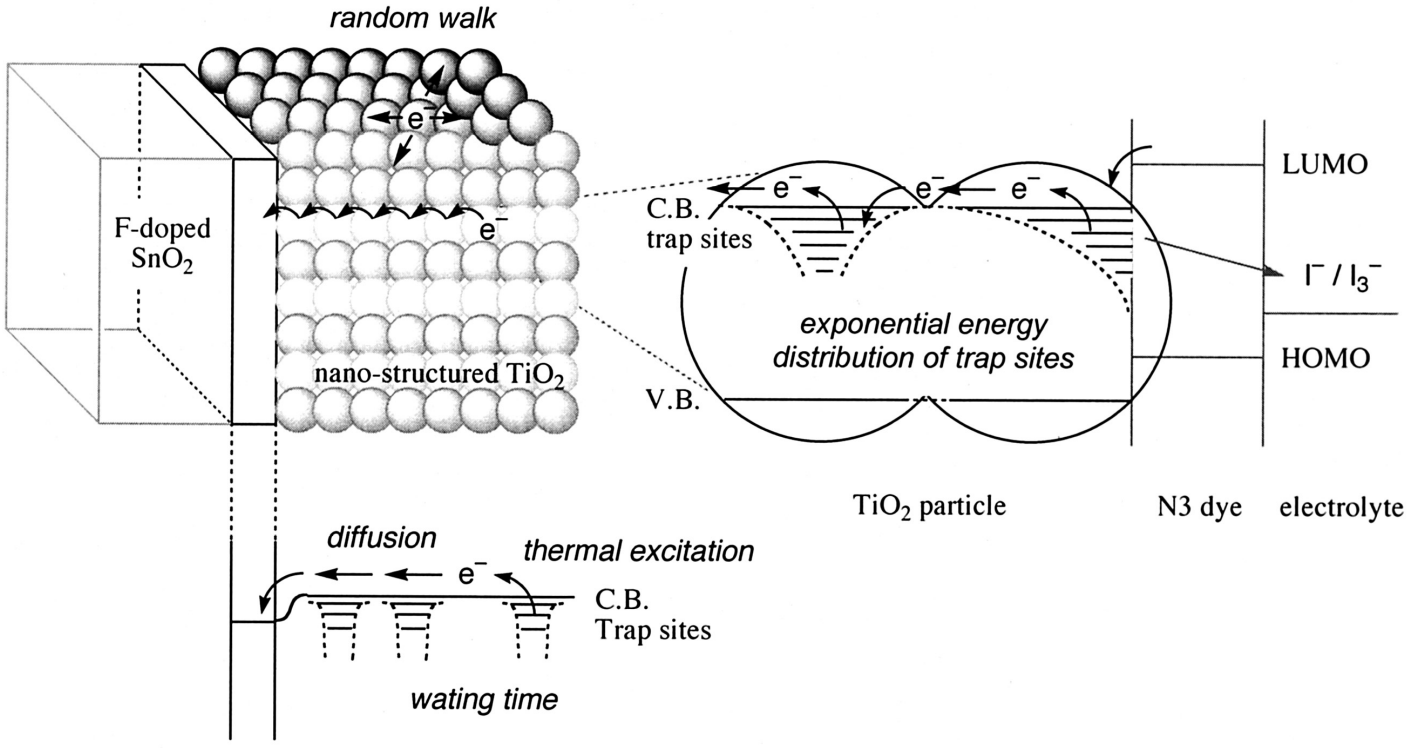

Fig. 2: Schematic view of electron transport mechanism in nano-structured TiO_2 electrode soaked in high ionic strength electrolyte.

electrons depends not only on the density of electrons but also on the concentration of ions in electrolytes such as lithium perchlorate ($LiClO_4$). The density of electrons is proportional to light intensity.

3.2. Evaluation method of electron diffusion in plain nano-structured TiO_2 layers

Electron diffusion in mesoporous TiO_2 films soaked in electrolyte was determined by laser-induced transient current measurements, which is a kind of time-of-flight technique [14,27–29]. When the electrode is illuminated by UV-light from the TiO_2–electrolyte interface side, only the shallow region of electrode surface is excited, since the absorption coefficient of TiO_2 in the UV region is large ($\sim 10^{-7}$ m^{-1}). The charge separation in the TiO_2 electrode after excitation is completed in the sub-nanosecond range. The hole at the valence band of TiO_2 is rapidly removed by supplying an electron from quenchers in solvent, suppressing initial electron–hole pair recombination inside the TiO_2. When a laser is employed as the excitation light source, electrons are generated at the shallow region of the electrolyte side of the TiO_2 electrode, and then travel to the substrate side by a diffusion process because of thermal fluctuations in the system. Therefore, with increasing thickness of the electrode the carriers travel a longer distance. The electron diffusion coefficient of the nano-structured TiO_2 electrode can be determined by analyzing the photocurrent transient response using Fick's diffusion model. Neglecting a current due to electrostatic repulsion in the solution of the time-dependent diffusion equation, the time for the current maximum, t_{peak}, appears when

$$t_{peak} = W^2/2D \tag{6}$$

where D is the electron diffusion coefficient, W is film thickness, and t_{peak} is the time of photocurrent maximum [27].

The nano-structured TiO_2 electrodes were prepared on transparent conducting glass (F-doped SnO_2) and annealed at 450°C for 30 min in air before the measurements. The electrodes were immersed in an ethanolic or acetonitrile electrolyte solution composed of $LiClO_4$, 0.7 M and using a platinum wire as a counter electrode. Short duration of excitation light was obtained using a 10 Hz Nd-YAG laser (The Quanta-Ray INDI Series Pulsed Nd : YAG Lasers, pulse width 7 ns, wavelength 355 nm) and time transient photocurrent was monitored by a digital oscilloscope (Tektronix TDS 3052, 500 MHz). The schematic picture is shown in Fig. 3. Filters were employed to prevent the effects of the 2-fold and 4-fold wavelength light. The density of photo-formed electrons in TiO_2 film, i.e., light intensity was controlled by using ND filters. The geometric area of an electrode was fixed as 0.093 cm^{-2} by an aperture. All the measurements were performed in air with at least 3-min intervals between measurements. Thickness of the films was measured by a Dectak profilometer and the surface roughness was about 5%.

3.3. Electron transport in nano-structured TiO_2 layers

Transient curves of the typical photocurrent observed for films having different thicknesses are shown in Fig. 4 [28]. The positions of the peaks in the current rise were shifted to longer times with increasing film thickness, indicating that the electrons have

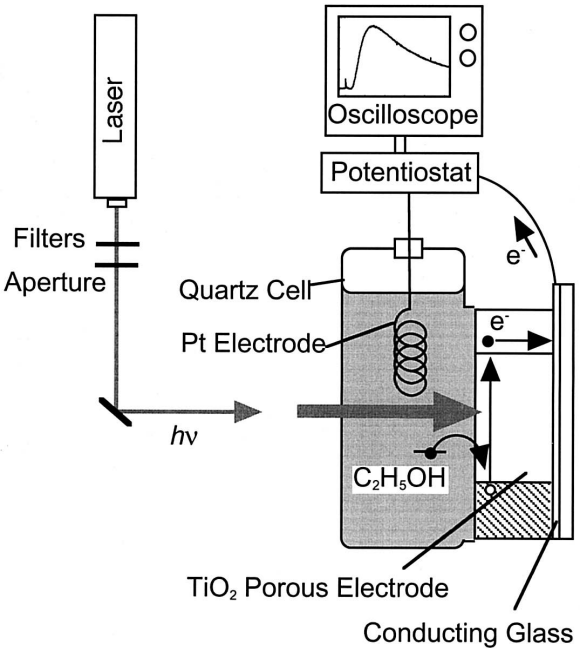

Fig. 3: The setup for measurement of the diffusion coefficient of electrons in nano-structured TiO_2.

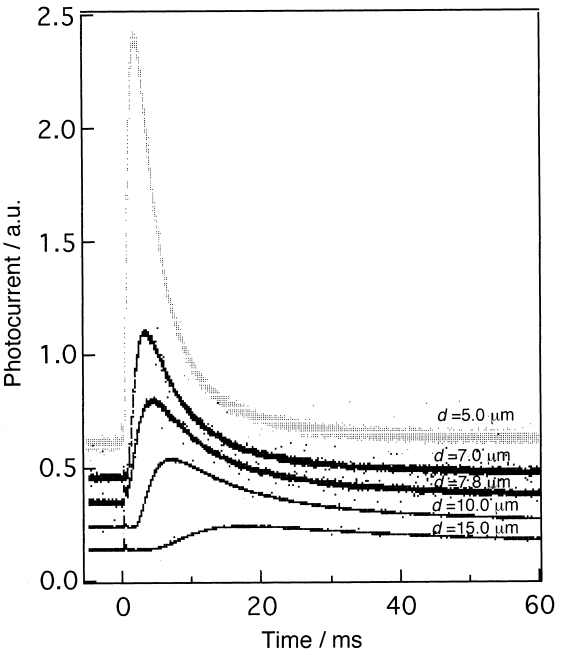

Fig. 4: Typical transient photocurrent observed for **A1** films with different thicknesses: Nd : YAG ($3\omega = 355$ nm), 7 ns, 0.98 mJ cm^{-2}, 0.093 cm^2.

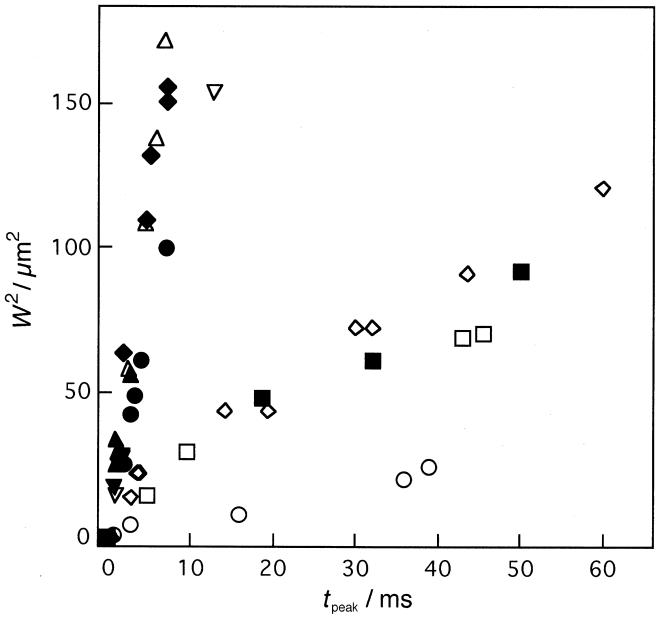

Fig. 5: The current peak vs. the square of each different nano-structured TiO_2 film thickness sintered at 450°C. **A1** (●), **A2** (■), **A3** (▲), **A4** (▼), **A5** (◆), **R1** (○), **R2** (□), **A5** containing 20 wt% of larger particles (△), **A2** sintered at 550°C (▽) and **R1** treated with $TiCl_4$ (◇).

to travel a longer distance to reach the conducting glass layer. The decay of the current was slower for the samples with larger thickness. Therefore, the experimental observations were qualitatively in agreement with those expected for the diffusive process of electrons in the films. The generated charge in our setup was evaluated as 1.2 μC for the electrode with 5 μm in thickness by integrating the transient curve between the times 0 and 100 ms and was almost constant for the films with $<$12 μm thickness, but decreased to 0.5 μC for those 15 μm in thickness. This is probably due to the back electron transfer to electron acceptors in the electrolyte solution such as oxidized ethanol, water, or dissolved oxygen.

We plotted W^2 vs. the peak time t_{peak} for the electrodes made with the TiO_2 samples according to the relationship expressed by Eq. 6 and obtained Fig. 5. A straight line was obtained for all of the examined nano-structured TiO_2 films, which indicates that the transport of electrons in the TiO_2 electrodes will follow the diffusion model.

The diffusion coefficients of electrons in nano-structured TiO_2 (D) were determined for comparing the electron transport properties of the TiO_2 films made with different TiO_2 nanoparticles [28] as follows. **A1** was anatase TiO_2 having spherical shape with an average size of 12 nm, which was prepared from titanium isopropoxide, containing a small amount of brookite crystal structure. **A2** was anatase TiO_2 having a higher crystallinity than **A1**. **A3** was phase-pure anatase TiO_2 having rod-like shape with an average size of 13 $\times$ 4 nm (supplied by Catalysis & Chemicals Industry (denoted as CCI, hereafter) HPW-25R). **A4** was phase-pure anatase having cubic shape with an

Table 1
Characteristics of TiO_2 nanoparticles and the electron diffusion coefficients of the electrodes

	Structure [a]	Shape	Size (nm) [b]	D ($\times 10^{-5}$ cm^2 s^{-1})
A1	A/Amor	Spheric	12	2.2
A1$_{TiCl_4}$ [c]	A/Amor	Spheric	12	2.2
A2	A	Cubic	12	0.3
A2$_{550}$ [d]	A	Cubic	12	2.0
A3 (CCI)	A	Rod-like	13/34	4.0
A4 (CCI)	A	Cubic	11	4.1
A5 (P25)	A/R	Spheric	21	4.0
A5$_{Large}$ [e]	A/R	Spheric	21	4.0
R1	R	Spheric	27	0.1
R1$_{TiCl_4}$ [c]	R	Spheric	27	0.4
R2 (CCI)	R	Rod-like	23/73	0.3

[a] A = anatase structure, Amor = amorphous phase, R = rutile structure.
[b] Average size.
[c] Treated with aq. $TiCl_4$ solution.
[d] Annealed at 550°C.
[e] With 20 wt% of large TiO_2 (Fluka).

average size of 11 nm (CCI, HPW-10R). **A5** was nano-structured TiO_2 (P25) having mixed crystal structure (anatase : rutile = 8 : 2), spherical shape and an average size of 21 nm (supplied by Nippon Aerosil). **R1** was rutile TiO_2 having spherical shape with average size 27 nm, which was prepared from titanium isopropoxide. **R2** was rutile crystal structure, rod-like shape and average size of 23 × 73 nm (CCI, HPR-16).

The D values determined for all the electrodes made from the TiO_2 samples are listed in Table 1. In general comparison, the electron diffusion coefficient of the rutile electrodes (D_{R1} and D_{R2}) was almost one order smaller than that of the anatase electrodes (D_{A1}, D_{A3}, D_{A4} and D_{A5}). Similar diffusion coefficients were obtained for **A3** and **A4** which were prepared by the common synthesis method, but possessed different particle sizes and shapes. The **A2** having the anatase structure but higher crystallinity than **A1** gave a smaller D value, but one which was highly increased by annealing at 550°C, being closed to that of D_{A1}.

The detailed comparison of the diffusion coefficient depending on the morphology of nano-structured TiO_2 film well indicates the importance of surface structure of anatase TiO_2 for fabrication of good electron transport layers of DSCs.

3.4. Effects of electrolytes on the electron transport

Ambipolar diffusion coefficients of electrons in nano-structured anatase TiO_2–electrolyte systems were determined in the presence of a wide range of concentrations of Li^+, Na^+, Mg^{2+}, tetrabutylammonium cation (TBA^+) or dimethylhexylimidazolium cation ($DMHI^+$) in electrolytes [29]. An imidazolium salt was examined as an electrolyte, because imidazolium cations are essential components to achieve high performance of dye-sensitized solar cells [30–32].

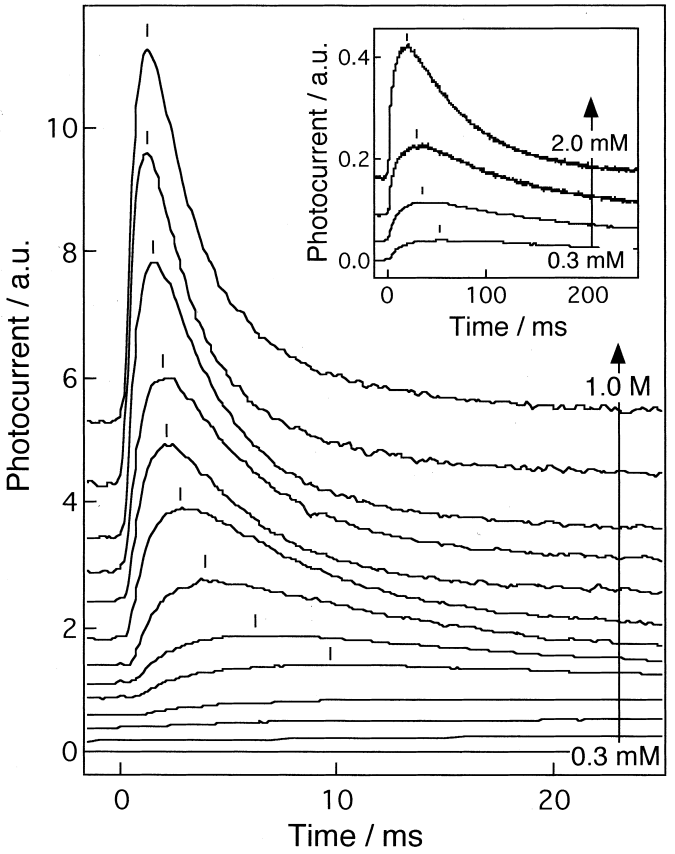

Fig. 6: Photocurrent transients for 7.2 μm-thick nano-structured TiO_2 electrodes in acetonitrile with various concentrations of $TBA^+ClO_4^-$ at average electron density $n = 2.1 \times 10^{17}$ cm^{-3}. From below 0.3, 0.7, 1.0, 2.0, 5.0, 10, 20, 40, 80, 100, 200, 500 and 1000 mM of the cation concentration. Inset shows longer time scale at low concentrations of TBA^+ from below 0.3, 0.7, 1.0 and 2.0 mM.

Fig. 6 shows the photocurrent transients in acetonitrile-electrolytes consisting of various densities of TBA^+ at a photoelectron density of $n = 2.1 \times 10^{17}$ cm^{-3}. The shape of photocurrent transients changed in the series and the peak of the photocurrent increased with an increase of TBA^+ density at a comparable photogenerated electron density. Fig. 7 shows the change in diffusion coefficient (D_{Amb}) as a function of TBA^+ density at different electron densities (n). A solid line obtained by fitting D_{Amb} according to Eq. 5 is shown in Fig. 7. The fitted curve of D_{Amb} agreed closely with the measured D_{Amb} at $D_n = 2.1 \times 10^{-4}$ cm^2 s^{-1} and $D_p = 2.8 \times 10^{-6}$ cm^2 s^{-1}. The D_p obtained by the curve fitting is close to the limiting cation diffusion coefficient $D_p^{\infty} = 2.32 \times 10^{-6}$ cm^2 s^{-1} derived from the Nernst equation using the limiting molar conductance $\Lambda_0 = 61.63$ S cm^2 mol^{-1} [33]. The diffusion coefficients (D_{Amb}) increase with an increasing cation density. Different n values give different D_{Amb}, and D_{Amb} was larger at higher n. This difference supports not only an ambipolar diffusion

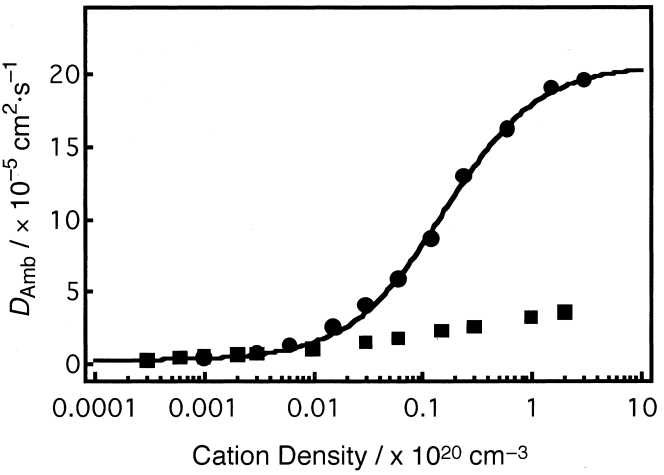

Fig. 7: Diffusion coefficients of electrons in nano-structured TiO_2 as a function of $TBA^+ClO_4^-$ density in acetonitrile at different electron densities n, 2.1×10^{17} cm^{-3} (•) and 5.0×10^{16} cm^{-3} (■). A line is calculated from Eq. 5 where $D_n = 2.1 \times 10^{-4}$ cm^2 s^{-1} and $D_p = 2.8 \times 10^{-6}$ cm^2 s^{-1}.

mechanism but also the trap-filling effect of electrons on electron transport in a DSC [12,13,22,34].

D_{Amb} as a function of the cation density was also determined for the case of Li^+, Na^+, Mg^{2+} and $DMHI^+$, as shown in Fig. 8. The D_{Amb} depends on kind of the cation and decreases in the order $DMHI^+ > TBA^+ > Na^+ > Li^+ > Mg^{2+}$. Interestingly, the diffusion coefficients increased drastically in the presence of highly concentrated Li^+ or $DMHI^+$ without fitting well with the ambipolar diffusion mechanism. These behaviors were in contrast with that in the case of TBA^+.

We have reported previously that the measured D was well interpreted with the ambipolar diffusion mechanism for a wide range of Li^+ densities in ethanolic electrolyte [27]. The difference observed in acetonitrile and in ethanol could be explained by the difference in Li^+ adsorption behavior on TiO_2. The adsorption of Li^+ in the TiO_2 electrodes increases the local cation density at the TiO_2 surface. And the results suggest that the adsorption might form favorable trap states in the surface TiO_2 and influences the electron transport.

The behavior of D_{Amb} as a function of the cation density in the case of $DMHI^+$ was similar to that in the case of Li^+ rather than TBA^+, although $DMHI^+$ is a quaternary ammonium cation. Taking into account the similarity of D_{Amb} in the case of $DMHI^+$ and Li^+, $DMHI^+$ adsorption on the TiO_2 was expected. While the adsorption of TBA^+ on TiO_2 (P25) surface was negligible, the estimated amount of the adsorbed $DMHI^+$ on the TiO_2 surface was ca. 100 molecules per nm^2, that is too large for a monolayer of $DMHI^+$ on the TiO_2, suggesting multi-layered adsorption of $DMHI^+$ on TiO_2. The proximity of multi-layered $DMHI^+$ to all particles on the surface causes screening of photoinjected electrons [20,35], leading to their enhanced transport.

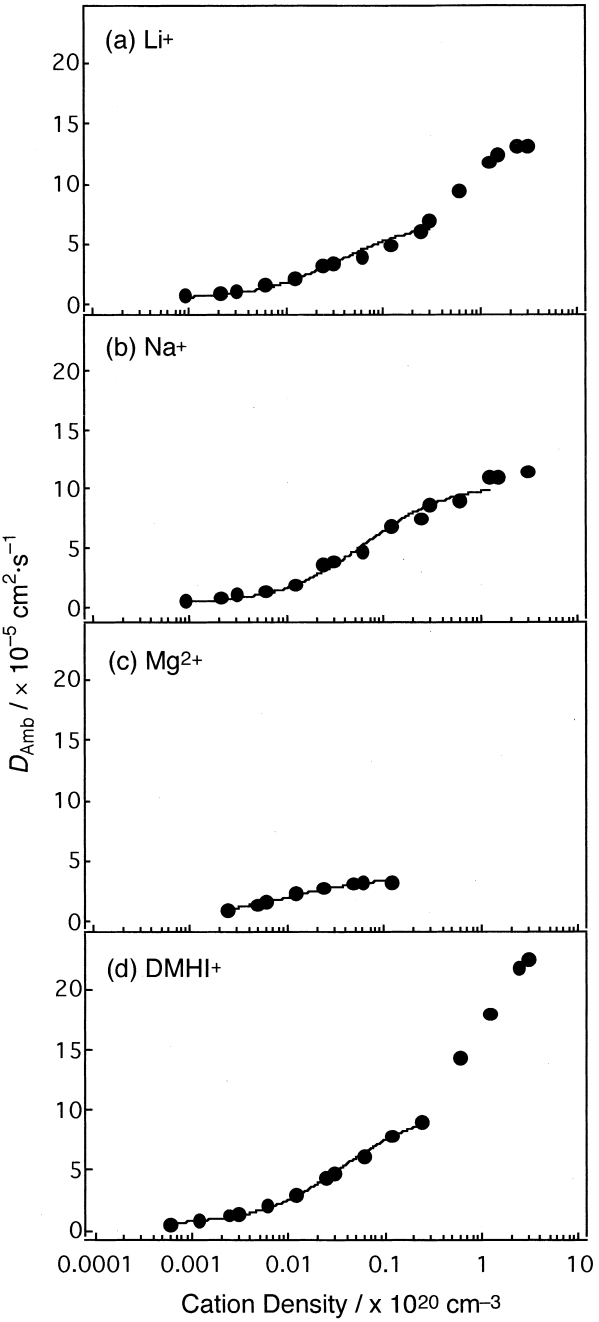

Fig. 8: Diffusion coefficients of electrons in nano-structured TiO_2 as a function of cation density of $LiClO_4$ (a), $NaClO_4$ (b), $Mg(ClO_4)_2$ (c) and $DMHI^+ClO_4^-$ (d) when $n = 2.1 \times 10^{17}$ cm^{-3} (Li^+), 1.6×10^{17} cm^{-3} (Na^+), 2.1×10^{17} cm^{-3} (Mg^{2+}) and 1.8×10^{17} cm^{-3} ($DMHI^+$) in acetonitrile. Lines are calculated from Eq. 5 at lower cation density.

3.5. Effect of surface states in nano-structured TiO_2

Positive introduction of oxygen vacancies or surface states as electron trapping site was expected to increase electron diffusion coefficients and to contribute to an increase of η_{et} of the TiO_2 films when they are formed just below the conduction band. The oxygen vacancies should originate from the 3d-orbital of Ti^{3+} but that is unstable in the presence of oxygen and water molecules. An alternative way to produce Ti^{3+} in the TiO_2 films is fluorine doping, i.e., the chemical replacement of O^{2-} with F^-. A high physical stability can be expected in the fluorine-doped TiO_2 films (TiO_2/F), because O^{2-} sites come to be occupied with the similar sized F^- [36,37]. Thus we applied a fluorine doped TiO_2 (TiO_2/F) to DSCs.

Fluorine-doped TiO_2 was synthesized by hydrolysis of $Ti(O^iPr)_4$ followed by autoclaving in the presence of HF. The content of fluorine in the doped particles was estimated as F/Ti = 0.0011 by applying the fundamental parameter method to the observed F-Kα signal on X-ray fluorescent analysis (Rigaku, ZSX100e; RX35 analyzing crystal; F-PC detector). The films (TiO_2/F) prepared in the similar procedure had the similar morphology to that of fluorine-free TiO_2. For comparison, TiO_2 films with excess oxygen vacancies were prepared by calcination under N_2 atmosphere, and the formation of oxygen vacancies was proved by absorption of UV-VIS spectroscopy at longer wavelength.

Laser pulse induced photocurrent measurements were performed under comparable conditions (in ethanolic solution of $LiClO_4$) for the TiO_2/F film and fluorine-free TiO_2 films with and without introduction of oxygen vacancies. Fig. 9 shows that the photocurrent transient is larger for the TiO_2/F film. The diffusion coefficients of the TiO_2/F film and the fluorine-free TiO_2 film were determined to be 1.5×10^{-4} cm^2 s^{-1} and 1.3×10^{-4} cm^2 s^{-1}, respectively. TiO_2 films with oxygen vacancies showed too poor current to determine the diffusion coefficient. Fig. 10 shows I–V curves of the cells fabricated by using these films with $\sim$4 μm thickness. Introduction of oxygen vacancies reduced photocurrent and photovoltage drastically but fluorine doping induced

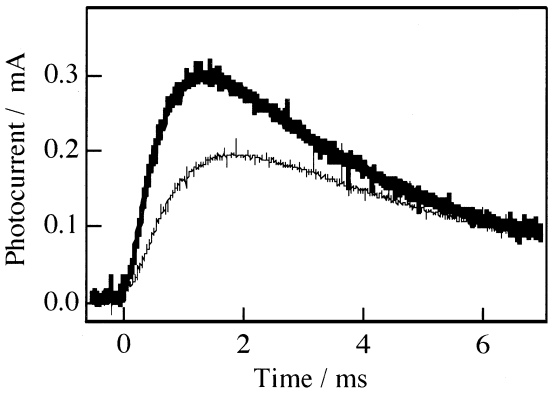

Fig. 9: Photocurrent transient induced by UV pulsed laser for 4.0 μm-thick TiO_2 (thin line) and TiO_2/F (bold line) in 0.7 M $LiClO_4$ ethanolic solution: Nd : YAG ($3\omega = 355$ nm), 6 ns, 15 μJ/0.02 cm^2.

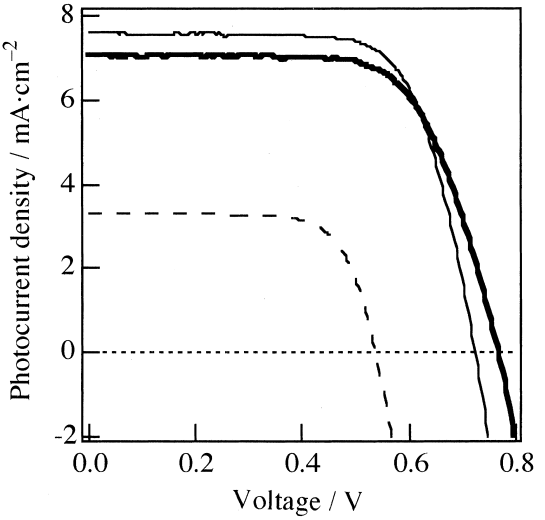

Fig. 10: Photocurrent density–voltage curve of dye-sensitized solar cells with 4 μm-thick nano-structured TiO_2 film under AM 1.5 irradiation: TiO_2 (thin line), TiO_2/F (bold line) and TiO_2 with excess oxygen vacancies (dashed line).

the increase of photovoltage [38]. These results suggest that while the oxygen vacancies may produce deep trap states as back electron transfer site, the doped fluorine states may serve as shallow trap sites just below the conduction band that might serve effective electron-transporting sites with a slight shift of the Fermi level to the negative.

4. Charge transport in iodide/polyiodide electrolytes of DSCs

4.1. Mechanistic studies using quasi-solid-state electrolytes produced by low-molecular-weight gelators

Quasi-solid-state DSCs were fabricated using low-molecular-weight gelators (Scheme 2) [39,40]. They showed comparable photoenergy conversion efficiencies to the liquid cell at high illumination intensity up to AM 1.5 (one sun). This fact implies the specific charge transport of the electrolytes of the iodine/iodide redox couple.

The employed electrolyte consisted of dimethylpropylimidazolium iodide (DMPImI), LiI, and I_2, and *tert*-butylpyridine (BP) as an additive and methoxypropylnitrile (MPN) as solvent. Conductivity measurements of the electrolyte phases revealed that the gelation does not affect largely the conductivity of the electrolyte and that the conductivity increased with an increase of iodine in both gel electrolytes and liquid electrolyte (Fig. 11). Raman spectroscopic measurements confirmed the formation of polyiodide ions (I^-_{2n+1}) such as I^-_3 and I^-_5 by addition of iodine. The self-diffusion of iodide species in the gel electrolyte was about a quarter of that of I^- in acetonitrile. Lindquist's group previously reported that the diffusion of I^-_{2n+1} in nano-structured TiO_2 space is one order

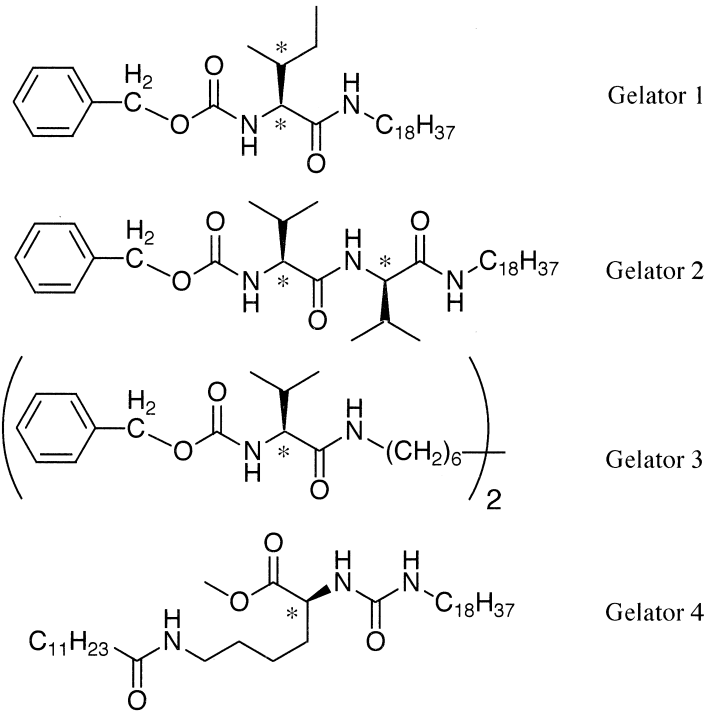

Scheme 2.

of magnitude lower than that in solution [41]. The less-mobile polyiodide ions in electrolyte did not influence the charge transport process, which is in contrast to the lower limiting molar conductivity of polyiodide species than monoiodide [33]. In addition, the rather high concentration (0.5 M) of polyiodide and iodide species in the electrolyte implies that such iodide species are located in the proximity of each other (~0.8 nm). These facts suggest that the effective charge transport in the electrolyte phase should be rationalized as due to electron hopping or iodine exchange (Grotthuss-type) mechanism caused by the rather packed polyiodide species in the electrolytes. Fig. 11 depicts the electronic transport in the iodide and polyiodide species in electrolyte. The effective electron injection (see Fig. 1) from iodide species to oxidized dye may suggest chemical interaction of polyiodide species and thiocyanide groups of the ruthenium dye molecule as shown in Fig. 12.

4.2. Quasi-solid stated DSCs using imidazolium molten iodides as electrolytes

In the measurement of the conductivity of the DSC's I^-/I_3^- redox electrolyte systems, the presence of imidazolium iodides instead of lithium iodide was found to increase the electron conductance of the redox electrolyte (Fig. 11) [40]. On the other hand, the presence of imidazolium cations accelerates the diffusion coefficient of electrons in the mesoporous TiO_2 phase (D_n) through their multi-layer adsorption [29]. In addition,

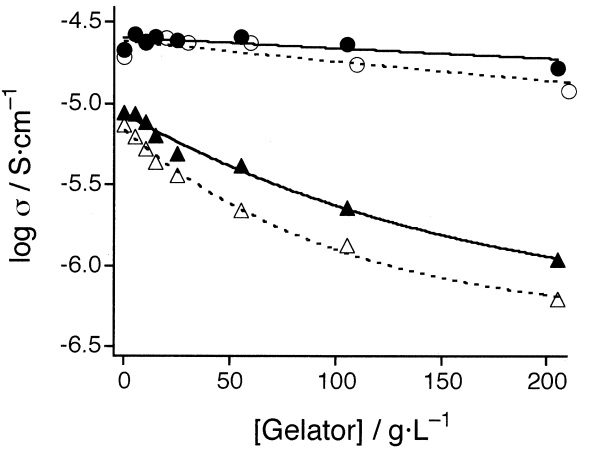

Fig. 11: Effect of the concentration of Gelator 2 on conductivity for electrolytes containing 0.5 M of iodide salts (DMPImI: ○, LiI: △) and electrolytes containing 0.5 M of iodide salts with 0.1 M of I_2 (DMPImI: ●, LiI: ▲).

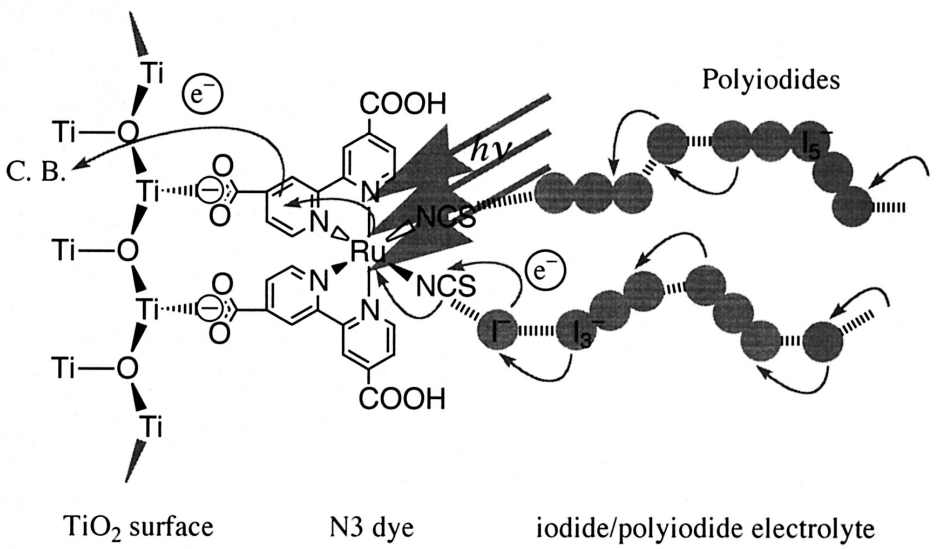

Fig. 12: Schematic view of interactions at the interfaces of nano-structured TiO_2/N3 and N3/iodide electrolyte and electron transport mechanism in iodide/polyiodide electrolyte.

some imidazolium iodides are known as chemically inert room-temperature molten salts, i.e., ionic liquids. Currently, many ionic liquids have attracted much attention as electrolyte in electrochemistry because of their features such as high ionic conductivity, non-volatility, thermal stability and non-flammability [42–44]. In fact, such imidazolium salts were applied to DSCs as non-volatile electrolyte solvent [31,45]. However, the

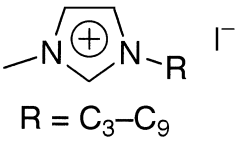

Scheme 3.

conversion efficiency of the cells showed lower than that of the cells using liquid electrolyte containing organic solvent.

When we applied 1-alkyl-3-methylimidazolium iodides (Scheme 3) to the electrolyte of DSCs by combining iodine but without using any volatile solvents, the electrolyte with 1-hexyl-3-methylimidazolium iodide gave respectable photoenergy conversion efficiency ($\eta = 5.0\%$) when combined with $1/10$ molarity of iodine. Further, solidification of the molten imidazolium salts using gelator (Scheme 2, Gelator 1) showed comparable conversion efficiency (5.0%) under AM 1.5 irradiation (Fig. 13) [46]. Under dry heat test, the quasi-solid-state imidazolium DSCs showed a higher stability than the quasi-solid-state DSCs fabricated using organic solvent with the same gelator [47]. It is interesting to note that the imidazolium DSC is non-flammable because of the high boiling point of the imidazolium salts as a room-temperature molten salt.

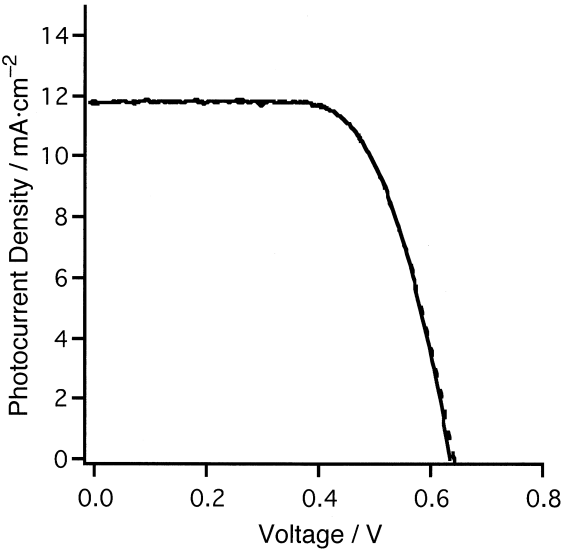

Fig. 13: Photocurrent–voltage curves of dye-sensitized solar cells with 1-hexyl-3-methylimidazolium iodide containing 8.7 wt% of I_2 under AM 1.5 irradiation without (dotted curve) and with (solid curve) 1.4 wt% of Gelator 1.

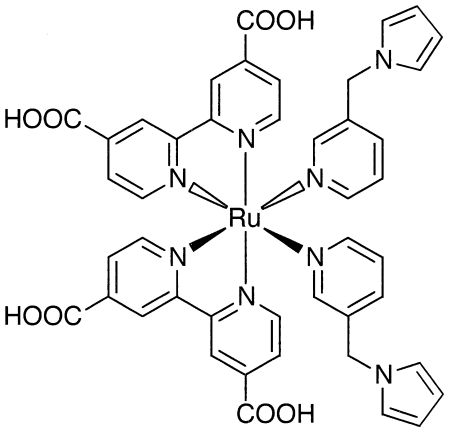

Scheme 4.

5. Importance of interface control in DSC fabrication

5.1. Interface structures affecting efficiencies, η_{ei} and η_{hi}

Dye adsorption on TiO_2 is important for fast electron injection in a dye-sensitization mechanism. In the case of N3/TiO_2 interface, the dye molecules are chemically adsorbed through one carboxylic group on each dcbpy ligand by an ether-like bond [48] or bidentate coordination [49] contributing to high efficiency of η_{ei}. The importance of a covalent bond between dye molecules and the hole transport layer was also displayed when polypyrrole (PPy) as a hole transport layer and a Ru dye with pyrrole group, *cis*-$Ru^{II}(dcbpy)_2(pmp)_2$, (pmp = 3-(pyrrole-1-ylmethyl)-pyridine; Scheme 4) were employed [50–52].

As for TiO_2 interface control, Huang et al. reported the suppression of back electron transfer to redox electrolytes by surface treatment with pyridine derivatives [53] or cholic acids [54,55]. Covering of solvent-exposed interface parts of OTE and TiO_2 surfaces by insulating molecules such as poly(phenylene oxide-*co*-2-allylphenylene oxide) or poly(methylsiloxane) contributes to a decrease of the back electron transfer [56].

5.2. Important role of interfaces affecting efficiencies, η_{ec} and η_{hc}

With regard to conducting window and counter electrodes, the conductivity relating to surface structures and morphology and the transparency especially at window OTE play some decisive roles. On the other hand, Willig pointed out the importance of the junction at window OTE (SnO_2/F) and nano-structured TiO_2 as a driving force of electron transfer in DSCs [20]. Gregg et al. reported the difference in role of metal deposition on window OTE in view of the work function [57]. These facts and findings are closely related with interfacial control affecting η_{ec}.

Fullerenes are good electron acceptors due to the small reorganization energy in

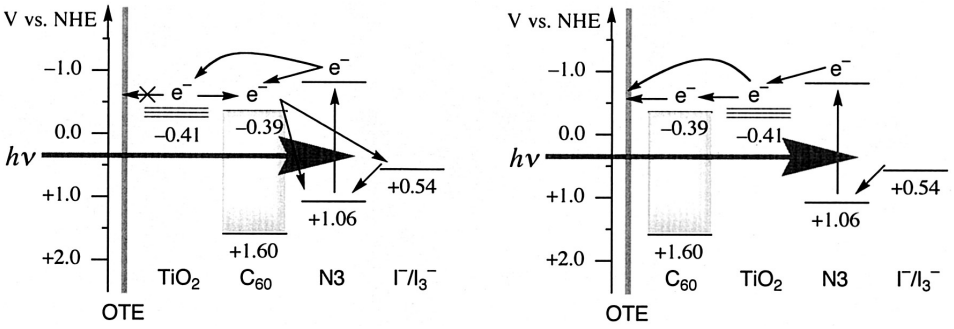

Scheme 5.

electron transfer and are applied to a variety of electron mediators in electron transfer reactions [58–60]. We successfully attempted to apply a C_{60} derivative to acceleration of electron capture at OTE in DSCs. Since the HOMO level of C_{60} is almost comparable to the conduction band of TiO_2, two systems, OTE/C_{60}/TiO_2/N3 and OTE/TiO_2/C_{60}/N3, were examined to know the role of C_{60} at interfaces of DSCs. As a C_{60} derivative, 1,2-methanato[60]-fullerene-61,61-dicarboxylic acid [61,62] was adsorbed on an OTE film or on OTE/TiO_2 film from toluene solution. The resulting OTE/C_{60} film was coated with nano-structured TiO_2 and sintered at 400°C for 30 min, and then N3 dye was adsorbed on the electrodes. The resulting OTE/C_{60}/TiO_2/N3 and OTE/TiO_2/C_{60}/N3 systems can be depicted as shown in the Scheme 5.

In the system of OTE/TiO_2/C_{60}/N3, the amount of the adsorbed dye molecules was decreased to about 40% of that of the OTE/TiO_2/N3 system fabricated as a reference system. On the other hand, the OTE/C_{60}/TiO_2/N3 system gave 80% dye-adsorption when compared to the OTE/TiO_2/N3 system. While negligible response in measurement of IPCE was observed in OTE/TiO_2/C_{60}/N3, the OTE/C_{60}/TiO_2/N3 system gave a response comparable to that of the OTE/TiO_2/N3 system in spite of the decrease of dye adsorption (Fig. 14). This result would suggest that C_{60} has a potential to mediate electron capture from TiO_2 to SnO_2/F, i.e., increase of η_{ec}.

Platinum or carbon deposition on counter OTE (SnO_2/F) electrode is known as a requisite in DSC fabrication in view of efficiency in hole capture at counter electrodes. In fabrication of solid state DSCs using polypyrrole as a hole transport layer and a Ru dye with pyrrole group, *cis*-$Ru^{II}(dcbpy)_2(pmp)_2$, carbon-based counter electrode improved cell performance compared to the cell with gold or platinum counter electrode [52]. A good electric contact of the hole transport layer of polypyrrole with the carbon electrode will enhance the efficiency η_{hc}.

6. Conclusions

The respectable conversion efficiency of Grätzel solar cells is now rationalized by 7 high efficiencies, i.e., light harvesting efficiency, electron injection, transport and capture efficiencies, and hole injection, transport and capture efficiencies. Interfacial structures

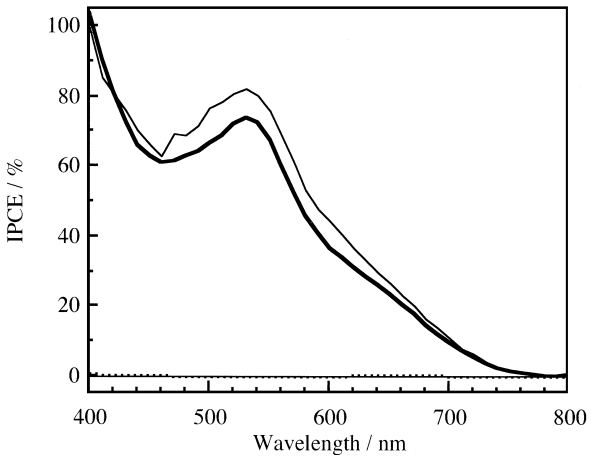

Fig. 14: IPCE spectra of dye-sensitized solar cells with 8.6 μm-thick TiO_2 (P25) film and N3 under AM 1.5 irradiation: OTE/TiO_2/N3 (thin line), OTE/C_{60}/TiO_2/N3 (bold line) and OTE/TiO_2/C_{60}/N3 (dashed line).

between nano-structured TiO_2, dye molecules, iodide/polyiodide couple, and window OTE and counter electrodes have influence on the efficiency for each step. For keeping good electron diffusion and charge transport both in TiO_2 and in iodide/polyiodide electrolyte, the presence of highly concentrated imidazolium species is favorable for DSC systems. Employment of a series of imidazolium iodides as ionic liquid electrolyte led to successful fabrication of DSCs with respectable efficiency and thermal stability when followed by solidification using a low-molecular-weight gelator.

Control of the interfaces to reduce the back electron transfer by chemically modifying the surfaces of TiO_2 and OTE materials is also an important subject to improve DSC performance. In the solidification of DSCs, we must maintain vectorial charge flow with keeping each efficiency optimal.

Acknowledgements

This work was partially supported by Grant-in-Aid for Scientific Research (A) (No. 11358006), and by Grant-in-Aid for the Development of Innovative Technology (No. 12310) from the Ministry of Education, Culture, Sports, Science and Technology of Japan.

References

1. B. O'Regan and M. Grätzel, Nature (London) **353**, 737 (1991).
2. M.K. Nazeeruddin, A. Kay, I. Rodicio, R. Humphry-Baker, E. Müller, P. Liska, N. Vlachopoulos, and M. Grätzel, J. Am. Chem. Soc. **115**, 6382 (1993).
3. M. Grätzel, Nature (London) **414**, 338 (2001).

4. Y. Tachibana, J.E. Moser, M. Grätzel, D.R. Klug, and J.R. Durrant, J. Phys. Chem. **100**, 20056 (1996).
5. T. Hannappel, B. Burfeindt, W. Storck, and F. Willig, J. Phys. Chem. B **101**, 6799 (1997).
6. J.S. Salafsky, W.H. Lubberhuizen, E. van Faassen, and R.E.I. Schropp, J. Phys. Chem. B **102**, 766 (1998).
7. S.A. Haque, Y. Tachibana, D.R. Klug, and J.R. Durrant, J. Phys. Chem. B **102**, 1745 (1998).
8. R.J. Ellingson, J.B. Asbury, S. Ferrere, H.N. Ghosh, J.R. Sprague, T. Lian, and A.J. Nozik, J. Phys. Chem. B **102**, 6455 (1998).
9. S.A. Haque, Y. Tachibana, R.L. Willis, J.E. Moser, M. Grätzel, D.R. Klug, and J.R. Durrant, J. Phys. Chem. B **104**, 538 (2000).
10. S.Y. Huang, G. Schlichthörl, A.J. Nozik, M. Grätzel, and A.J. Frank, J. Phys. Chem. B **101**, 2576 (1997).
11. S. Södergren, A. Hagfeldt, J. Olsson, and S.-E. Lindquist, J. Phys. Chem. **98**, 5552 (1994).
12. F. Cao, G. Oskam, G.J. Meyer, and P.C. Searson, J. Phys. Chem. **100**, 17021 (1996).
13. P.E. de Jongh and D. Vanmaekelbergh, Phys. Rev. Lett. **77**, 3427 (1996).
14. A. Solbrand, H. Lindström, H. Rensmo, A. Hagfeldt, S.-E. Lindquist, and S. Södergren, J. Phys. Chem. B **101**, 2514 (1997).
15. G. Schlichthörl, S.Y. Huang, J. Sprague, and A.J. Frank, J. Phys. Chem. B **101**, 8141 (1997).
16. L. Dloczik, O. Ileperuma, I. Lauermann, L.M. Peter, E.A. Ponomarev, G. Redmond, N.J. Shaw, and I. Uhlendorf, J. Phys. Chem. B **101**, 10281 (1997).
17. G. Franco, J. Gehring, L.M. Peter, E.A. Ponomarev, and I. Uhlendorf, J. Phys. Chem. B **103**, 692 (1999).
18. G. Schlichthörl, N.G. Park, and A.J. Frank, J. Phys. Chem. B **103**, 782 (1999).
19. A. Solbrand, A. Henningsson, S. Södergren, H. Lindström, A. Hagfeldt, and S.-E. Lindquist, J. Phys. Chem. B **103**, 1078 (1999).
20. K. Schwarzburg and F. Willig, J. Phys. Chem. B **103**, 5743 (1999).
21. J. Nelson, Phys. Rev. B **59**, 15374 (1999).
22. A.C. Fisher, L.M. Peter, E.A. Ponomarev, A.B. Walker, and K.G.U. Wijayantha, J. Phys. Chem. B **104**, 949 (2000).
23. N. Kopidakis, E.A. Schiff, N.-G. Park, J. van de Lagemaat, and A.J. Frank, J. Phys. Chem. B **104**, 3930 (2000).
24. J. van de Lagemaat and A.J. Frank, J. Phys. Chem. B **104**, 4292 (2000).
25. J. van de Lagemaat, N.-G. Park, and A. J. Frank, J. Phys. Chem. B **104**, 2044 (2000).
26. J. Nelson, S.A. Haque, D.R. Klug, and J.R. Durrant, Phys. Rev. B **63**, 205321 (2001).
27. S. Nakade, S. Kambe, T. Kitamura, Y. Wada, and S. Yanagida, J. Phys. Chem. B **105**, 9150 (2001).
28. S. Kambe, S. Nakade, Y. Wada, T. Kitamura, and S. Yanagida, J. Mater. Chem. **12**, 723 (2002).
29. S. Kambe, S. Nakade, T. Kitamura, Y. Wada, and S. Yanagida, J. Phys. Chem. B **106**, 2967 (2002).
30. C.J. Barbé, F. Arendse, P. Comte, M. Jirousek, F. Lenzmann, V. Shklover, and M. Grätzel, J. Am. Ceram. Soc. **80**, 3157 (1997).
31. N. Papageorgiou, Y. Athanassov, M. Armand, P. Banhôte, H. Pettersson, A. Azam, and M. Grätzel, J. Electrochem. Soc. **143**, 3099 (1996).
32. P. Banhôte, A.-P. Dias, M. Armand, N. Papageorgiou, K. Kalyanasundaram, and M. Grätzel, Inorg. Chem. **35**, 1168 (1996).
33. J. Berthel, L. Iberl, J. Rossmaier, H.J. Gores, and B. Kaukal, J. Solut. Chem. **19**, 321 (1990).
34. K. Schwarzburg and F. Willig, Appl. Phys. Lett. **58**, 2520 (1991).
35. D. Cahen, G. Hodes, M. Grätzel, J.F. Guillemoles, and I. Riess, J. Phys. Chem. B **104**, 2053 (2000).
36. S.N. Subbarao, T.H. Yun, R. Kershaw, K. Dwight, and A. Wold, Mat. Res. Bull. **13**, 1461 (1978).
37. S.N. Subbarao, T.H. Yun, R. Kershaw, K. Dwight, and A. Wold, Inorg. Chem. **18**, 488 (1979).
38. S. Yamagida, T. Kitamura, and M. Kohmoto, Electrochem. **70**, 399 (2002).
39. W. Kubo, K. Murakoshi, T. Kitamura, Y. Wada, K. Hanabusa, H. Shirai, and S. Yanagida, Chem. Lett., 1241 (1998).
40. W. Kubo, K. Murakoshi, T. Kitamura, S. Yoshida, M. Haruki, K. Hanabusa, H. Shirai, Y. Wada, and S. Yanagida, J. Phys. Chem. B **105**, 12809 (2001).

41. Z. Kebede and S.-E. Lindquist, Solar Energy Mater. Solar Cells **51**, 291 (1998).
42. R. Hagiwara and Y. Ito, J. Fluorine Chem. **105**, 221 (2000).
43. T. Welton, Chem. Rev. **99**, 2071 (1999).
44. A.B. McEwen, H.L. Ngo, K. LeCompte, and J.L. Goldman, J. Electrochem. Soc. **146**, 1687 (1999).
45. H. Matsumoto, T. Matsuda, T. Tsuda, R. Hagiwara, Y. Ito, and Y. Miyazaki, Chem. Lett., 26 (2001).
46. W. Kubo, T. Kitamura, K. Hanabusa, Y. Wada, and S. Yanagida, Chem. Commun., 374 (2002).
47. Japanese Industrial Standard, Environmental and endurance test methods for amorphous solar cell modules, JIS C 8938, (1995).
48. K. Murakoshi, G. Kano, Y. Wada, S. Yanagida, H. Miyazaki, M. Matsumoto, and S. Murasawa, J. Electroanal. Chem. **396**, 27 (1995).
49. K.S. Finnie, J.R. Bartlett, and J.L. Woolfrey, Langmuir **14**, 2744 (1998).
50. K. Murakoshi, R. Kogure, Y. Wada, and S. Yanagida, Chem. Lett., 471 (1997).
51. K. Murakoshi, R. Kogure, Y. Wada, and S. Yanagida, Solar Energy Mater. Solar Cells **55**, 113 (1998).
52. T. Kitamura, M. Maitani, M. Matsuda, Y. Wada, and S. Yanagida, Chem. Lett., 1054 (2001).
53. S.Y. Huang, G. Schlichthörl, A.J. Nozik, M. Grätzel, and A.J. Frank, J. Phys. Chem. B **101**, 2576 (1997).
54. A. Kay and M. Grätzel, J. Phys. Chem. **97**, 6272 (1993).
55. K. Hara, H. Sugihara, Y. Tachibana, A. Islam, M. Yanagida, K. Sayama, H. Arakawa, G. Fujihashi, T. Horiguchi, and T. Kinoshita, Langmuir **17**, 5992 (2001).
56. B.A. Gregg, F. Pichot, S. Ferrere, and C.L. Fields, J. Phys. Chem. B **105**, 1422 (2001).
57. F. Pichot and B.A. Gregg, J. Phys. Chem. B **104**, 6 (2000).
58. H. Imahori, K. Hagiwara, M. Aoki, T. Akiyama, S. Taniguchi, T. Okada, M. Shirakawa, and Y. Sakata, J. Am. Chem. Soc. **118**, 11771 (1996).
59. M. Knupfer, Surface Sci. Rep. **42**, 1 (2001).
60. N.S. Sariciftci, Prog. Quant. Electr. **19**, 131 (1995).
61. X. Campas and A. Hirsch, J. Chem. Soc. Perkin Trans. 1, 1595 (1997).
62. I. Lamparth, G. Schick, and A. Hirsch, Liebigs Ann./Recueil, 253 (1997).